



# PCCP

## Ligand Field Effects on the Ground and Excited States of Reactive FeO<sub>2</sub><sup>+</sup> Species

Journal:	<i>Physical Chemistry Chemical Physics</i>
Manuscript ID	CP-ART-08-2018-005372.R2
Article Type:	Paper
Date Submitted by the Author:	19-Oct-2018
Complete List of Authors:	Kirkland, Justin; University of Tennessee, Department of Chemistry Khan, Shahriar; Auburn University, Chemistry and Biochemistry Casale, Bryan; University of Tennessee, Department of Chemistry Miliordos, Evangelos; Auburn University, Chemistry and Biochemistry Vogiatzis, Konstantinos; University of Tennessee, Department of Chemistry

SCHOLARONE™  
Manuscripts



Journal Name

ARTICLE

## Ligand Field Effects on the Ground and Excited States of Reactive FeO<sup>2+</sup> Species

Received 00th January 20xx,  
Accepted 00th January 20xx

Justin K. Kirkland,<sup>a</sup> Shahriar N. Khan,<sup>b</sup> Bryan Casale,<sup>a</sup> Evangelos Miliordos<sup>\*b</sup> and Konstantinos D. Vogiatzis<sup>\*a</sup>

DOI: 10.1039/x0xx00000x

[www.rsc.org/](http://www.rsc.org/)

High-valent Fe(IV)-oxo species have been found to be key oxidizing intermediates in the mechanisms of mononuclear iron heme and non-heme enzymes that can functionalize strong C-H bonds. Biomimetic Fe(IV)-oxo molecular complexes have been successfully synthesized and characterized, but their catalytic reactivity is typically lower than the enzymatic analogues. The C-H activation step proceeds through two competitive mechanisms, named  $\sigma$ - and  $\pi$ -channels. We have performed high-level wave function theory calculations on bare FeO<sup>2+</sup> and a series of non-heme Fe(IV)-oxo model complexes in order to elucidate the electronic properties and the ligand field effects on those channels. Our results suggest that a coordination environment formed by a weak field gives access to both competitive channels, yielding more reactive Fe(IV)-oxo sites. On the contrary, a strong ligand environment stabilizes only the  $\sigma$ -channel. Our concluding remarks will aid on the derivation of new structure-reactivity descriptors that can contribute on the development of the next generation of functional catalysts.

### I. Introduction

The selective functionalization of the C-H bond has been regarded as a problem of major interest for energy and industrial applications.<sup>1-4</sup> This process is present in many biological processes and is promoted by enzymes that contain metal-oxo active sites. Nature has developed a large variety of heme and non-heme enzymes for the controlled oxidation of organic substrates.<sup>5,6</sup> Enzymes containing mononuclear and dinuclear iron sites activate dioxygen and form intermediate metal-oxo species, which promote the functionalization of strong C-H bonds.<sup>6,7</sup> For example, the non-heme enzymes  $\alpha$ -ketoglutarate dependent taurine dioxygenase (TauD)<sup>8,9</sup> and syringomycin halogenase (SyrB2)<sup>10,11</sup> form high-valent Fe(IV)-oxo intermediates which can abstract a H-atom from an inert C-H bond as strong as 106 kcal/mol to initiate hydroxylation or halogenation.<sup>12-15</sup>

In an attempt to mimic nature and obtain new insights on the reactivity of the Fe(IV)-oxo unit, many non-heme Fe(IV)-oxo model complexes have been synthesized and characterized.<sup>16-20</sup> Alternatively, zeolites and metal-organic frameworks (MOFs) provide coordination environments suitable for the stabilization of highly reactive intermediates. Cationic Fe complexes stabilized in zeolite or MOFs micropores have been shown to be efficient catalysts for the selective oxyfunctionalization of

methane and ethane.<sup>21-25</sup> For these cases, a Fe(IV)-oxo intermediate has been suggested as the reactive intermediate.<sup>23,24</sup>

From an electronic structure standpoint, nature shows preference to a coordination environment for Fe(IV)-oxo which promote the highly reactive high-spin quintet state ( $S = 2$ ). Porous materials produce a weak ligand field on the deposited iron cations which stabilizes the high-spin intermediate as verified by magnetic circular dichroism (MCD) spectroscopy<sup>23</sup> and computational studies.<sup>24,26,27</sup> On the other hand, the synthetic non-heme model complexes tend to prefer an intermediate spin state (triplet state;  $S = 1$ ).<sup>16,17,28</sup> Several attempts have been made to synthesize stable high-spin models,<sup>29-35</sup> such as the tridentate TMG<sub>3</sub>tren (TMG<sub>3</sub>tren = 1,1,1-tris[2-[N2-(1,1,3,3-tetramethylguanidino)]ethyl]amine) Fe(IV)-oxo complex.<sup>29</sup>

Triplet spin complexes typically follow a two-state reactivity (TSR) scheme switching from triplet to quintet along the hydrogen abstraction step which lowers the activation barrier.<sup>36</sup> This spin-flip has been argued to have an energy penalty that lowers the reactivity of the  $S = 1$  complexes.<sup>37</sup> Alternatively, Meyer and co-workers applied a strong ligand field using a tetracarbene ligand maximizing the triplet-quintet gap.<sup>38-41</sup> This complex was found to be more reactive than other synthetic  $S = 1$  non-heme model complexes and was attributed to the avoidance of the TSR scheme.

Aside from the spin issue, low catalytic reactivity of most of the model complexes is attributed to two other key reasons: the steric hindrance of the active sites, and the self-oxidation pathways that they undergo. MCD spectroscopy and multiconfigurational wave function theory calculations have revealed two different reaction channels for the [Fe<sup>IV</sup>(O)(TMG<sub>3</sub>tren)]<sup>2+</sup> complex.<sup>42</sup> The first one activates a C-H

<sup>a</sup> Department of Chemistry, University of Tennessee, Knoxville, Tennessee 37996, United States.

<sup>b</sup> Department of Chemistry and Biochemistry, Auburn University, Auburn, Alabama 36849, United States.

Electronic Supplementary Information (ESI) available: Details on the multiconfigurational calculations (excited states, examination of different active spaces), cartesian coordinates. See DOI: 10.1039/x0xx00000x

bond of the substrate, and leads to the formation of the desired product, whereas the second one self-oxidizes the ligand and is responsible for the self-decay of the catalyst.

In total, four possible reaction channels are considered depending on the spin state of the Fe(IV)-oxo and the molecular

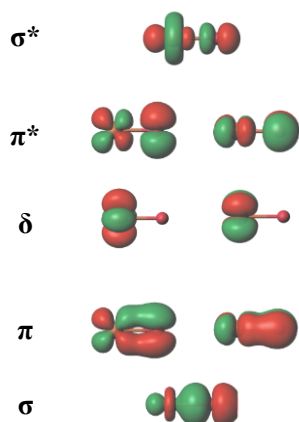


Figure 1: Valence molecular orbitals of bare  $\text{FeO}^{2+}$  ( $R_{\text{Fe-O}} = 1.64 \text{ \AA}$ ).

orbital (MO) that overlaps with the activated C-H bond, which consequently leads to the abstraction of the hydrogen atom. Previous studies have described the electronic structure of ground and excited states of several Fe(IV)-oxo species.<sup>39,40,42-46</sup> These electronic states can be further related to different C-H activation mechanisms, and involve the evolution of Fe(IV)-O<sup>2-</sup> (oxo) to Fe(III)-O<sup>•</sup> (oxyl), which occur upon elongation of the Fe-O bond.<sup>47</sup> The valence molecular orbitals ( $\sigma$ ,  $\pi$ ,  $\delta$ ,  $\pi^*$ ,  $\sigma^*$ ) of the Fe-O unit are shown in Figure 1 denoted by  $\sigma$ ,  $\pi$ ,  $\delta$  ( $d_{x^2-y^2}/d_{xy}$ ),  $\pi^*$ , and  $\sigma^*$ . The first reaction channel involves the excitation of an electron from the  $\sigma$  bonding orbital (polarized towards oxygen) to the  $\sigma^*$  antibonding orbital (polarized towards iron). Therefore, upon the  $\sigma \rightarrow \sigma^*$  excitation, the  $2p_z$  orbital of the oxygen atom becomes singly occupied, and O<sup>2-</sup> evolves the radical O<sup>•</sup> (oxyl) character. The hydrogen atom abstraction via the  $2p_z$  ( $\sigma$ ) orbital is termed as  $\sigma$ -mechanism and it is accessed from the ground state of the Fe(IV)-oxo intermediate. The first, doubly degenerate excited state introduces a competitive mechanism where one of the degenerate  $2p_{x/y}$  orbitals of the oxygen atom (polarized  $\pi$  orbital) becomes singly occupied and the oxo atom evolves a radical O<sup>•</sup> character. Since the  $2p_{x/y}$  orbitals are involved in the  $\pi/\pi^*$  molecular orbitals, this C-H activation channel is termed as  $\pi$ -mechanism. The  $\sigma$ - and  $\pi$ -channels can further be divided to triplet  $^3\sigma$  and  $^3\pi$  and quintet  $^5\sigma$  and  $^5\pi$ , depending the spin state of the Fe(VI)-oxo unit. Figure 2 presents all four mechanisms with MO diagrams, which suggest that the  $^5\sigma/^5\pi$  mechanisms should be favored under a near-trigonal pyramidal field whereas  $^3\sigma/^3\pi$  mechanisms are more likely for near-octahedral structures.

Overall the followed mechanism is determined by the combination of specific electronic and stereochemical conditions. For example, the  $S = 1$  species undergoing a TSR mechanism prefer the  $^5\sigma$  channel,<sup>48</sup> while the high reactivity of the  $S = 1$  tetracarbene complex is because of the accessibility to both  $^3\sigma$  and  $^3\pi$  channels (about 4 kcal/mol difference).<sup>40</sup> The

high-spin ( $S = 2$ ) trigonal bipyramidal  $[\text{Fe}^{\text{IV}}(\text{O})(\text{TMG}_3\text{tren})]^{2+}$  complex has also multiple available channels ( $^5\sigma$ ,  $^5\pi$ ,  $^3\pi$ ) but shows reactivity comparable to  $S = 1$  complexes undergoing a TSR mechanism.<sup>29</sup> The reason is that unlike  $^5\sigma$ , the  $^5\pi$ ,  $^3\pi$  channels cause the self-oxidation of the complex due to preferential overlap of the  $2p_{x/y}$  orbitals of oxygen with the methyl groups of the ligands.<sup>42,49</sup> It is noteworthy that the non-heme enzyme SyrB2 modulates its reactivity by different channels; hydroxylation proceeds via  $^5\sigma$ , while halogenation via  $^5\pi$ .<sup>11,43</sup> Finally, the stereochemistry of the active site and the reactants promotes both  $^5\pi$  and  $^5\sigma$  mechanisms for the C-H activation of 4-hydroxymandelate synthase (HmaS) and (4-hydroxyphenyl)pyruvate dioxygenase (HPPD), and AlkB enzymes.<sup>50,51</sup>

Presently, we aim to systematically analyze the electronic factors favoring the different reaction channels facilitated by the Fe(IV)-oxo sites. Our target is to elucidate at the electronic structure level how the ligand field increases or decreases the accessibility of each reactive channel. To this end, we performed multiconfigurational quantum chemical calculations for the ground and low-lying electronic states of model  $[\text{FeO}]^{2+}$  systems. We started by constructing potential energy profiles for bare  $[\text{FeO}]^{2+}$  followed by the singly coordinated  $[(\text{H}_3\text{N})\text{FeO}]^{2+}$  and  $[(\text{H}_2\text{O})\text{FeO}]^{2+}$  species before the study of the larger penta- and hexa-coordinated complexes composed of ammonia and water ligands in different ratios. We found that strong field ligands enable only the  $^5\sigma$  mechanism, while weak ligands expedite additional channels.

The computational methodology followed in this study is described in Section II. In Section III, the low-lying energy states of bare and mono-coordinated  $[\text{FeO}]^{2+}$  are discussed in detail. Section IV focuses on the ligand field effects on the reactive lowest lying electronic states. The electronic structure of each state is analyzed and correlated to the different reaction channels. Finally, in Section V, we summarize our findings and make suggestions for designing new ligands that can increase the accessibility of specific reaction channels or for descriptors.

## II. Computational Methodology

To ensure the accurate description of the  $S = 1$  and  $S = 2$  radical nature, we employed various multiconfigurational wave function approaches. The complete active space self-consistent field (CASSCF)<sup>52,53</sup> method was used to obtain the reference wave function. The notation CAS( $n,m$ ) stands for  $n$  electrons allocated in  $m$  active orbitals. Dynamical correlation was added by means of internally contracted multireference configuration interaction (MRCI)<sup>54,55</sup> or second-order perturbation theory (CASPT2).<sup>56</sup>

For diatomic  $[\text{FeO}]^{2+}$ , all possible singly and doubly excitations of all valence electrons to the virtual space were variationally coupled through the internally contracted MRCI scheme implemented in MOLPRO.<sup>57</sup> The reference CASSCF wave function was built by allocating the  $4s3d/\text{Fe } 2p/\text{O}$  electrons

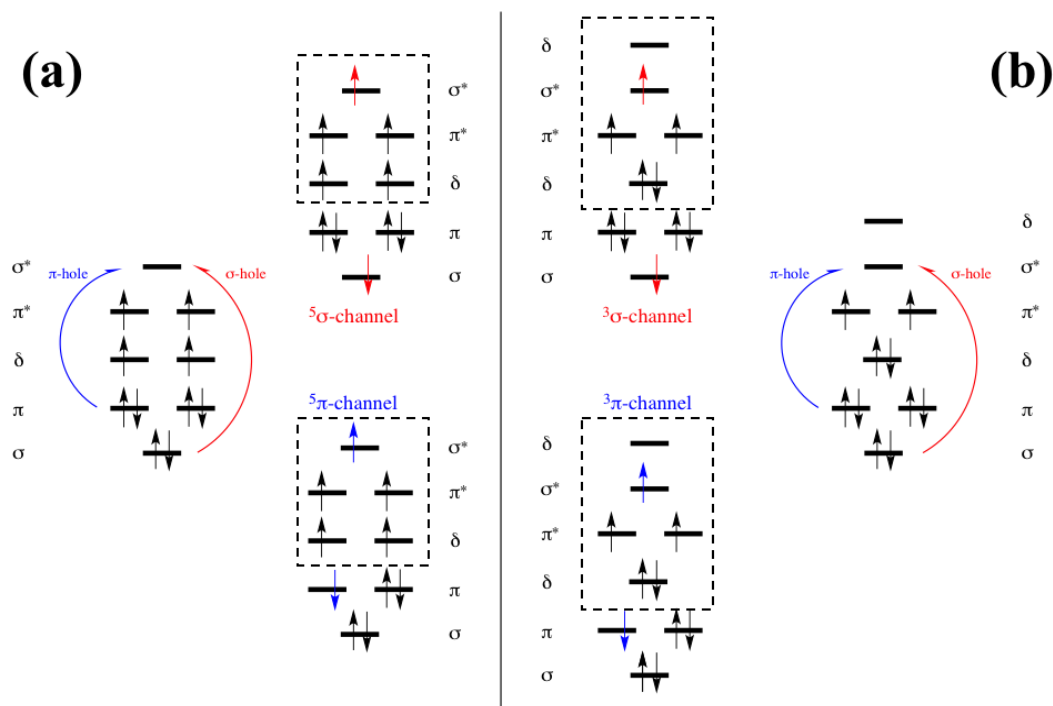


Figure 2: Molecular orbital diagram for (a) high-spin  $S = 2$  Fe(IV)-oxo species in a near-trigonal pyramidal field and (b) intermediate-spin  $S = 1$  Fe(IV)-oxo species in a near-tetragonal pyramidal field. Curvy arrows show the electron transferred upon Fe-O bond elongation for the formation of the Fe(III)-oxyl species that promote the hydrogen atom abstraction via (a) the  $5\sigma$  and  $5\pi$  channels and (b) the  $3\sigma$  and  $3\pi$  channels. Orbitals inside the dashed-line boxes have predominant iron character.

in 14 orbitals which at infinite Fe-O separation correspond to the  $4s3d_{\text{Fe}} 2p_{\text{O}}$  orbitals plus an additional series of five d-orbitals on iron (CAS(12,14)). The latter ones were deemed technically necessary for the correct dissociation of the potential energy curves (PECs). The cc-pVQZ/Fe aug-cc-pVQZ/O basis set was used to construct the CASSCF orbitals. State-averaged calculations were performed with all states having equal weights.

The calculations for the singly coordinated  $[(\text{H}_3\text{N})\text{FeO}]^{2+}$  and  $[(\text{H}_2\text{O})\text{FeO}]^{2+}$  complexes were done in the equilibrium region using only the  $4s3d_{\text{Fe}} 2p_{\text{O}}$  orbitals in the reference CASSCF wave function (CAS(12,9)), but still allowing excitations from all valence orbitals at MRCI.

Larger active spaces had to be considered for the larger complexes. For the near- $C_{4v}$  hexa-coordinated and near- $C_{3v}$  penta-coordinated iron complexes, one and two bonding ligand-Fe( $3d_{x^2-y^2}$ ) and ligand-Fe( $3d_{xy}/3d_{x^2-y^2}$ ) MOs were added, respectively (the term *near* is used since consideration of hydrogen atoms of the ligands lowers the symmetry of the tetragonal pyramidal and trigonal pyramidal, respectively). In the latter case, the displacement of 2s of oxygen by a ligand orbital was observed at specific Fe-O bond distances. This orbital rotation didn't affect the quintet states, but introduced inconsistencies for triplets. The second d-shell of Fe was found to affect the relative energy differences by less than 0.1 eV (see ESI, Section S1) and it was excluded. The total size of the active space is CAS(20,13) and CAS(18,12) for penta- and hexacoordinated Fe complexes, respectively. State-averaged restricted active space SCF (SA-RASSCF)<sup>52,58</sup> calculations were performed for the examination of larger active spaces that

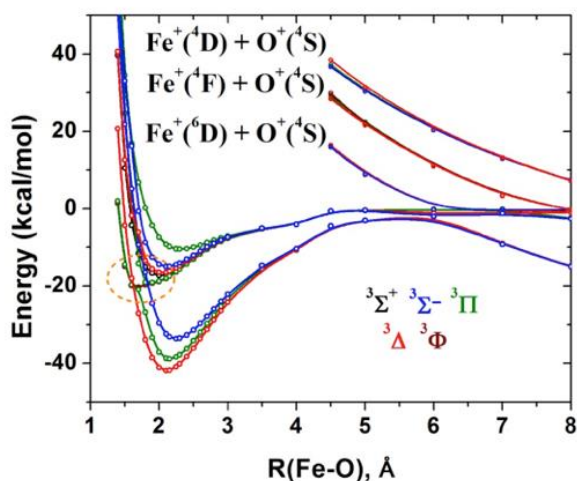
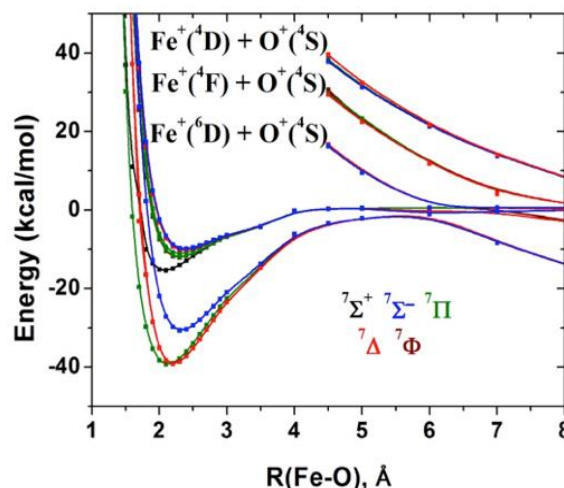
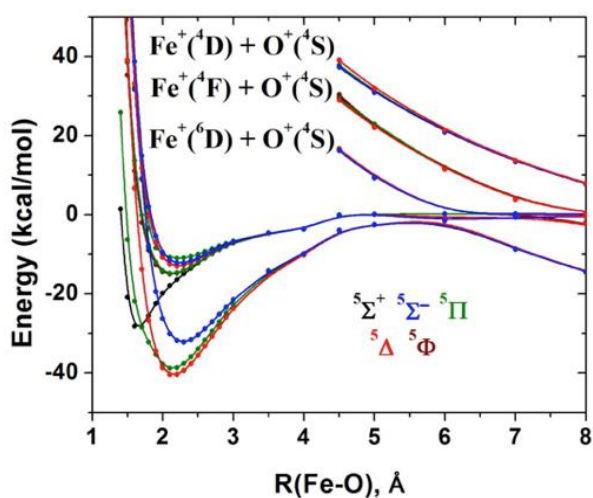
included the 3s of Fe, the 2s of O, and lone pair of  $\text{NH}_3$ , as it is discussed in the ESI, Sections S1-S2. For quantitative results, the multi-state extension of CASSCF and RASSCF that include dynamic correlation from second-order perturbation theory (CASPT2<sup>56</sup> and RASPT2<sup>59</sup>, respectively) were used.

All SA-RASSCF/MS-RASPT2 calculations were performed with the MOLCAS 8.2 program package.<sup>60</sup> Scalar relativistic effects were included using the all-electron triple-zeta quality atomic natural orbital relativistic basis sets (ANO-RCC-VTZP)<sup>61,62</sup> and a second-order Douglas-Kroll-Hess Hamiltonian.<sup>63,64</sup> A shifted zeroth-order Hamiltonian<sup>65</sup> (IPEA shift) with the default value of 0.25 a.u. and an imaginary shift<sup>66</sup> of 0.2 a.u. were applied to all MS-RASPT2 calculations. The two-electron integral evaluation was simplified by using the Cholesky decomposition.<sup>67</sup>

### III. Bare and mono-coordinated $[\text{FeO}]^{2+}$

We start our discussion with the bare and mono-coordinated  $[\text{FeO}]^{2+}$  species since they provide valuable insights which aid the investigation of the larger systems. It should be mentioned that the electronic structure of the bare FeO and  $[\text{FeO}]^+$  has been examined previously in great detail,<sup>68,69</sup> but to the best of our knowledge, bare  $[\text{FeO}]^{2+}$  has not been studied before.

The first two ionization energies of iron are 7.90 eV [ $\text{Fe}(5\text{D}) \rightarrow \text{Fe}^+(6\text{D})$ ] and 16.19 eV [ $\text{Fe}^+(6\text{D}) \rightarrow \text{Fe}^{2+}(5\text{D})$ ],<sup>70</sup> while for oxygen they are 13.62 eV [ $\text{O}(3\text{P}) \rightarrow \text{O}^+(4\text{S})$ ] and 35.12 eV [ $\text{O}^+(4\text{S}) \rightarrow \text{O}^{2+}(3\text{P})$ ].<sup>70</sup> These values set the lowest dissociation channel as  $\text{Fe}^+(6\text{D}) + \text{O}^+(4\text{S})$  followed by  $\text{Fe}^{2+}(5\text{D};\text{d}^6) + \text{O}(3\text{P})$  at 2.57 eV. This energy range fits eight excited electronic states of

Figure 3: Potential energy curves of the triplet electronic states of  $\text{FeO}^{2+}$ .Figure 5: Potential energy curves of the septet electronic states of  $\text{FeO}^{2+}$ .Figure 4: Potential energy curves of the quintet electronic states of  $\text{FeO}^{2+}$ .

$\text{Fe}^+$ ,<sup>71</sup> but none for  $\text{O}^+$ . All  $\text{Fe}^+ + \text{O}^+(4\text{S}; 2s^2 2p^3)$  asymptotes generate dissociative PECs, and considering a  $1/R(\text{Fe-O})$  repulsion the  $\text{Fe}^+ + \text{O}^+$  energies increase by as much as 1.44 eV at 10 Å. At the same distance, the  $\text{Fe}^{2+} + \text{O}$  fragments interact only weakly. Thus, the  $\text{Fe}^+(6\text{D}) + \text{O}^+(4\text{S})$  and  $\text{Fe}^{2+}(5\text{D}; d^6) + \text{O}(3\text{P})$  asymptotes approach to  $2.57 - 1.44 = 1.13$  eV, which means that only three  $\text{Fe}^+ + \text{O}^+$  channels are lower than  $\text{Fe}^{2+} + \text{O}$  at 10 Å. All states (32 triplets, quintets, and septets) of these four channels are included in our PECs of Figures 3-5 which cover Fe-O distances shorter than 8 Å. Further implying this simple model, the  $\text{Fe}^+(6\text{D}) + \text{O}^+(4\text{S})$  and  $\text{Fe}^{2+}(5\text{D}; d^6) + \text{O}(3\text{P})$  asymptotes are expected to cross at  $1/R(\text{Fe-O}) = 2.57$  eV which yields  $R(\text{Fe-O}) = 5.6$  Å. Indeed our PECs present an avoided crossing region at 5.5-6 Å. Setting the zero of the energy scale equal to that of  $\text{Fe}^{2+}(5\text{D}) + \text{O}(3\text{P})$ , the lowest energy fragments  $\text{Fe}^+(6\text{D}) + \text{O}^+(4\text{S})$  are at  $-2.57$  eV =  $-59.3$  kcal/mol. In the same scale the equilibrium energy of the ground  $3\Delta$  state is  $-42$  kcal/mol (see Figure 3) and  $-10$  kcal/mol for our highest state ( $3\Pi$ ). Therefore, all equilibrium energies are lower than the  $\text{Fe}^{2+} + \text{O}$  fragments but higher than the  $\text{Fe}^+ + \text{O}^+$  ones, which means that bare  $\text{FeO}^{2+}$

is thermodynamically unstable, but kinetically stable because of the large dissociation barriers.

The first three dissociation paths associate with the  $6\text{D}$  ( $4s^1 3d^6$ ),  $4\text{F}$  ( $3d^7$ ), and  $4\text{D}$  ( $4s^1 3d^6$ ) states of  $\text{Fe}^+$  which combined with  $\text{O}^+(4\text{S})$  create a series of singlets, triplets, quintets, and septets with  $\Sigma^+$ ,  $\Sigma^-$ ,  $\Pi$ ,  $\Delta$ , and  $\Phi$  symmetries. The  $\text{Fe}^{2+}(5\text{D}) + \text{O}(3\text{P})$  channel generates (Wigner-Witmer rules) the  $^{3,5,7}[\Sigma^+, \Sigma^-(2), \Pi(3), \Delta(2), \Phi]$  states. The states of the same spin and space symmetry from the different channels run into each other producing the avoided crossings of Figures 3-5.

All minima at Fe-O distances of 2-2.5 Å are coming smoothly from  $\text{Fe}^{2+}(5\text{D}) + \text{O}(3\text{P})$  and their equilibrium electronic structure is closer to the Fe(III)-oxyl picture. For example,  $5\Delta$  at its equilibrium bond length of 2.15 Å is (see ESI)  $|^5\Delta\rangle \approx 0.72 |\sigma^2 \pi^2 \pi^{*2} \delta^3 \sigma^{*1}\rangle$ . However, there are PECs which exhibit additional features. Specifically, the  $5\Sigma^+$  state of Figure 4 follows its sister states for distances longer than 2.5 Å tending to form a minimum at 2.2 Å. It deviates though creating a minimum at 1.64 Å. Similar minima are found for  $3\Phi$  and  $3\Sigma^+$  which undergo an avoided crossing right at the region of their 1.6 Å minima (see the encircled region of Figure 3). Finally,  $5\Pi$  reveals a shoulder at the same distance (see Fig), which turns out to create gradually a clear minimum in the presence of ligands (see below). The electronic configurations and spectroscopic constants for all of the bound states are given in the ESI, Section S3.

To locate the origin of these additional features we focused on the CI vectors at 1.6 Å of the relative states. The dominant electronic configuration of  $5\Sigma^+$  (equilibrium) and  $5\Pi$  (shoulder), are (see Figure 1 for orbital notation):

$$|^5\Sigma^+\rangle \approx 0.74 |\sigma^2 \pi^4 \pi^{*2} \delta^2\rangle$$

$$|^5\Pi\rangle \approx 0.78 |\sigma^2 \pi^4 \pi^{*1} \delta^2 \sigma^{*1}\rangle$$

These are the only quintets with  $\sigma^2 \pi^4$ , and as discussed in the introduction, the polarization of  $\sigma$  and  $\pi$  towards oxygen signals an *in situ* Fe(IV)-oxo picture. All quintets with equilibrium bond lengths of about 2-2.5 Å are of  $\sigma^2 \pi^4$  or  $\sigma^2 \pi^3$  character matching better to a radical terminal oxygen, Fe(III)-oxyl. The same

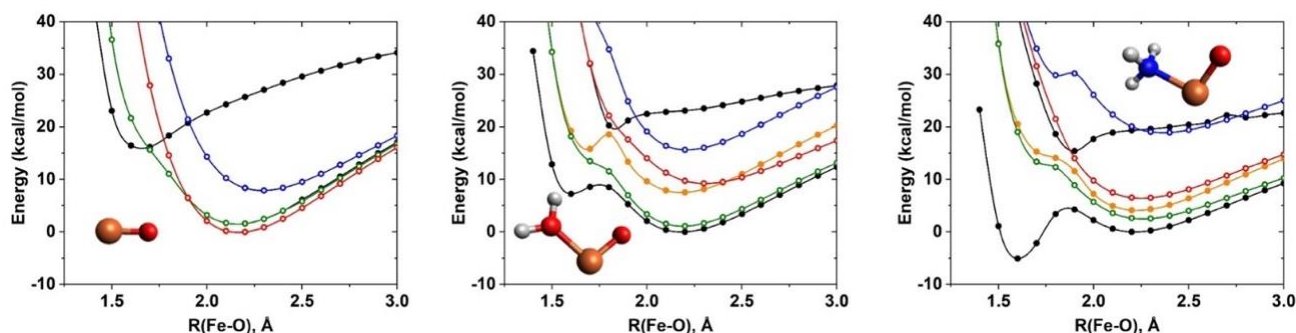


Figure 6: CASSCF(12,9)/MRCI PECs for  $[\text{FeO}]^{2+}$ ,  $[(\text{H}_2\text{O})\text{FeO}]^{2+}$ , and  $[(\text{H}_3\text{N})\text{FeO}]^{2+}$  using the cc-pVTZ (Fe,  $\text{NH}_3$ ,  $\text{H}_2\text{O}$ ) aug-cc-pVQZ (terminal O) basis set. The color coding for bare  $\text{FeO}^{2+}$  is the same as in Figure 4. For the mono-coordinated complexes, solid circles correspond to  ${}^5\text{A}'$  and open circles to  ${}^5\text{A}''$  states

configurations prevail for  ${}^5\Sigma^+$  and  ${}^5\Pi$   $R(\text{Fe-O}) > 2.0$  Å. Specifically, their configurations at 2.7 Å ( ${}^5\Sigma^+$ ) and 2.14 Å ( ${}^5\Pi$ ) are:

$$|{}^5\Sigma^+\rangle \approx 0.80 |\sigma^1\pi^4\pi^*2\delta^2\sigma^*1\rangle$$

$$|{}^5\Pi\rangle \approx 0.72 |\sigma^2\pi^3\pi^*2\delta^2\sigma^*1\rangle$$

Because of their larger iron formal charge, the approach of a ligand is expected to stabilize the equilibrium of  ${}^5\Sigma^+$  and the shoulder of  ${}^5\Pi$  over the rest quintets.

To corroborate these observations, we added an ammonia or water ligand to the  $[\text{FeO}]^{2+}$  diatomic and constructed the PECs in the Fe-O equilibrium region for the lowest quintet states ( ${}^5\Sigma^+$ ,  ${}^5\Pi$ ,  ${}^5\Delta$ ). The  $[\text{FeO}(\text{H}_2\text{O})]^{2+}$  and  $[\text{FeO}(\text{H}_3\text{N})]^{2+}$  structures were fully optimized at the MRCI level for the  ${}^5\Sigma^+$  and then scanned over the Fe-O distance by keeping all other geometrical parameters fixed. The potential energy curves are shown in Figure 6.

In comparison to bare  $[\text{FeO}]^{2+}$ , the  ${}^5\Sigma^+$  minimum (black line) is stabilized with the addition of a water molecule (weak ligand field), and even more so with an ammonia molecule (strong ligand field). The same is true for the shoulder of  ${}^5\Pi$  which splits into two components due to symmetry lowering. In the case of ammonia, one of the  ${}^5\Pi$  components becomes a very shallow local minimum. It is these minima that stabilize further upon the addition of more ligands generating the  ${}^5\text{A}$  and  ${}^5\text{E}$  states (see Section IV). Overall, the  ${}^5\Sigma^+$  and  ${}^5\Pi$  states have a Fe(IV)-oxo character at  $R(\text{Fe-O}) \sim 1.6$  Å which switches to Fe(III)-oxyl at  $R(\text{Fe-O}) \sim 2.25$  Å. This transition occurs at about 1.8 Å (energy barrier of the two rightmost plots of Figure 6). Additionally, The Fe(IV)-oxo region is stabilized over the Fe(III)-oxyl region when adding a ligand, and this stabilization is larger for ammonia than water.

These observations generally apply to the corresponding  ${}^5\text{A}$  and  ${}^5\text{E}$  states of the fully coordinated systems examined in Section IV, where more accurate and quantitative results are reported. To assure that CASPT2, which was used for the larger complexes, and MRCI are equivalent, we repeated the above analysis for the diatomic  $[\text{FeO}]^{2+}$  species at the SA(3)-CASSCF/MS(3)-CASPT2 level; MRCI and CASPT2 are in agreement with each other.

#### IV. Ligand Field Effects

The effect of different ligand fields on the stability of the larger fully-coordinated Fe(IV)-oxo species and its evolution to

the reactive Fe(III)-oxyl are discussed in this Section. The six different model complexes used in this study are the  $[\text{Fe}(\text{O})(\text{H}_2\text{O})_4]^{2+}$ ,  $[\text{Fe}(\text{O})(\text{H}_2\text{O})_5]^{2+}$ ,  $[\text{Fe}(\text{O})(\text{H}_2\text{O})_{\text{ax}}(\text{NH}_3)_3]^{2+}$ ,  $[\text{Fe}(\text{O})(\text{H}_2\text{O})_{\text{ax}}(\text{NH}_3)_4]^{2+}$ ,  $[\text{Fe}(\text{O})(\text{NH}_3)_4]^{2+}$ , and  $[\text{Fe}(\text{O})(\text{NH}_3)_5]^{2+}$  (Figure 7). The  $\text{H}_2\text{O}$  ligands are considered representative of a weak ligand field, while the  $\text{NH}_3$  ligands representative of a strong ligand field. Two out of these six models ( $[\text{Fe}(\text{O})(\text{H}_2\text{O})_5]^{2+}$  and  $[\text{Fe}(\text{O})(\text{H}_2\text{O})_{\text{ax}}(\text{NH}_3)_4]^{2+}$ ) have been employed by Kazaryan and Baerends<sup>72</sup>, who examined using density functional theory (DFT) the ligand field effects on the spin state and the C-H activation promoted by the Fe(IV)-oxo moiety. The Fe atom in the  $[\text{Fe}(\text{O})(\text{H}_2\text{O})_5]^{2+}$  model experiences a weak field and has a  $S = 2$  ground spin state. On the contrary, the  $[\text{Fe}(\text{O})(\text{H}_2\text{O})_{\text{ax}}(\text{NH}_3)_4]^{2+}$  model has a  $S = 1$  ground state, since the  $\text{NH}_3$  ligands form a stronger field. The  $[\text{Fe}(\text{O})(\text{H}_2\text{O})_{\text{ax}}(\text{NH}_3)_4]^{2+}$  model is also representative of the two-state reactivity scheme for the C-H activation mechanism, since a spin-transition occurs at the corresponding transition state.<sup>36</sup> However, CASPT2 calculations on the DFT optimized geometries predicted for both systems a high-spin  $S = 2$  ground spin state. For obtaining optimized geometries with the correct ground state for all six model complexes, we have performed symmetric Fe-L scans ( $L = \text{equatorial H}_2\text{O}$  or  $\text{NH}_3$ ). For the models with strong ligand fields, the addition of the lone pair of  $\text{NH}_3$  and the  $3s3p$  of Fe was mandatory.<sup>73,74</sup> The MS-RASPT2 calculations provided the correct global ground spin state ( $S = 1$ ) for the pseudo- $C_{4v}$  species ( $[\text{Fe}(\text{O})(\text{H}_2\text{O})_{\text{ax}}(\text{NH}_3)_4]^{2+}$ ), as expected, with a Fe-L distance of 2.000 Å. Similarly, the expected high-spin ( $S = 2$ ) was obtained for the remaining pseudo- $C_{3v}$  models ( $[\text{Fe}(\text{O})(\text{H}_2\text{O})_{\text{ax}}(\text{NH}_3)_3]^{2+}$  and  $[\text{Fe}(\text{O})(\text{NH}_3)_4]^{2+}$ ), as it is explained in the introduction. Figures with the six potential energy scans along the Fe-L distances are given in ESI, Section S1.

Once the equatorial Fe-L distances were calibrated for the six models, potential energy curves along the Fe-O bond distance were calculated. A detailed analysis of one representative species ( $[\text{Fe}(\text{O})(\text{H}_2\text{O})_5]^{2+}$ ) is given, but similar considerations hold for the remaining five models (ESI, Section S4). The left plot of Figure 8 shows the potential energy curves for the ground ( ${}^5\text{A}$ , orange) and the doubly degenerate first excited state ( ${}^5\text{E}$ , black), calculated at the MS-RASPT2(24,15) level of theory. A detailed analysis of the CI coefficients obtained from the multiconfigurational zeroth-order SA-

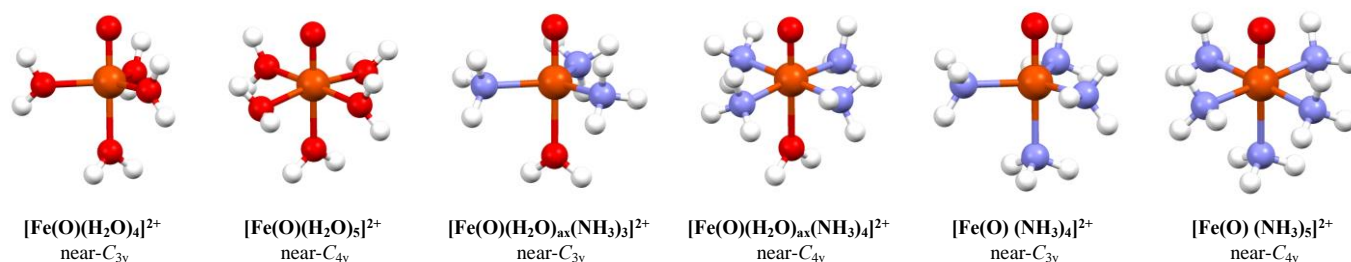


Figure 7: The six model complexes used in this work, their chemical formula and their pseudo-symmetry point group. The Fe-equatorial ligand distances have been optimized with symmetric scans at the CASSCF/RASSCF level. (Fe: light brown, O: red, N: blue, H: white).

CASSCF(18,12) wave function reveals the character of the two electronic states. As it is explained in Section 1 and shown in Figure 2, the non-reactive Fe(IV)-oxo configuration involves a  $3d^4$  Fe and a closed-shell  $2p^6$  O atom. By adding the weights (i.e. the square of the CI coefficients) of each configuration that corresponds to such electronic configurations, we can calculate the Fe(IV)-oxo character of each state. Similarly, the reactive Fe(III)-oxyl character can be calculated as the sum of all configurations that involve the transfer of an electron from O to Fe.

This electron transfer reduces Fe(IV) to Fe(III) and creates a hole in the electronic configuration of the O atom, which results to the radical character of the oxyl species. At the equilibrium bond distance (around 1.58 Å), both states have a non-reactive character, with a 0.73/0.14 ratio between Fe(IV)-oxo/Fe(III)-oxyl for the ground state  $^5A$  and 0.54/0.30 ratio for the first excited state  $^5E$ , as it is shown on the right plot of Figure 8. The character of the two states changes upon Fe-O bond elongation. It is evident from the same plot of Figure 8 that at 1.67 Å, the reactive Fe(III)-oxyl becomes the dominant character of the first excited state. This means that the  $\pi$ -channel becomes accessible at bond distances of 1.67 Å or higher. However, the excited state is still less stable than the  $^5A$  state by about 1eV (Figure, 8 left). The  $^5A$  ground state obtains a radical character at about 1.84 Å, and the  $\sigma$ -channel becomes accessible. The intercrossing of the two states occurs at about 1.86 Å and thus, both reactive channels are accessible for C-H abstraction. The Fe-O bond distance at the transition state of the C-H activation is expected to fall between 1.67 Å and 1.86 Å. Indeed, previous

mechanistic DFT studies for a fully hydrated  $\text{FeO}^{2+}$  species predicted a Fe-O distance at the transition state of 1.728 Å<sup>72</sup>, while for the fully oxygen coordination sphere of a Fe-containing MOF-74 catalyst, a value of 1.75 Å was calculated.<sup>26</sup>

The triplet states for the  $[\text{Fe}(\text{O})(\text{H}_2\text{O})_5]^{2+}$  model complex were calculated at the same level of theory (MS-CASPT2(18,12), see ESI, Section S4). The relative energy of the six lowest states from the  $^5A$  ground state is more than 1.73 eV at the equilibrium geometry, where they exhibit a shallow minimum in their potential energy curves. Similarly to the quintet counterparts, they have a non-reactive Fe(IV)-oxo character that evolves into radical Fe(III)-oxyl at longer Fe-O bond distances. Their energies at the  $R_{\text{Fe-O}} = 1.7$ -1.9 Å range are between 1.0-1.3 eV, comparable to the quintet states (Figure 8, left). This leads to the conclusion that the triplet channels are also accessible for C-H activation, in addition to the quintet  $\sigma$ - and  $\pi$ -channels. We were not able to distinguish between the  $^3\sigma$ - and  $^3\pi$ -channels since electronic configurations corresponding to these channels were present in all low-lying triplet states. Exception was the  $[\text{Fe}(\text{O})(\text{H}_2\text{O})_{\text{ax}}(\text{NH}_3)_4]^{2+}$  species, as it is discussed in the next paragraphs.

The results from all six model complexes are summarized in . The first observation is related to the relative energy differences of the quintet ground and excited states (also shown in Figure 9). For the two hydrated models (four and five water molecules in the coordination sphere of Fe), the relative energy differences of the two states at 1.60 Å is 1.31 and 1.24 eV, respectively. The same energy difference increases once the equatorial water molecules are substituted by stronger ligands

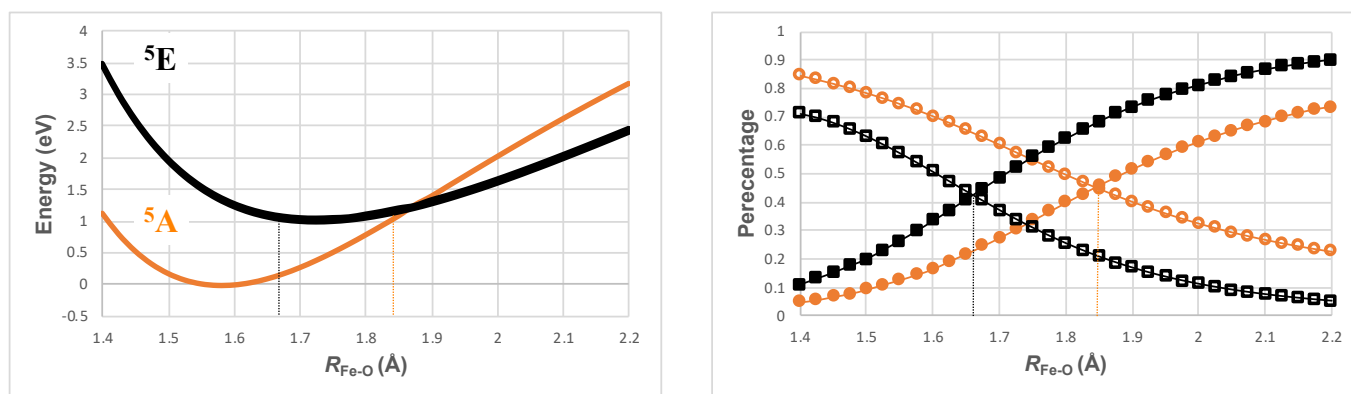


Figure 8: Left: Potential energy curves of  $[\text{Fe}(\text{O})(\text{H}_2\text{O})_5]^{2+}$  at the MS-CASPT2(18,12) level for the ground ( $^5A$ , orange) and first excited state ( $^5E$ , black) along the Fe-O bond distance. Right: The percentage of the wave function for the ground ( $^5A$ , orange) and first excited state ( $^5E$ , black) along the Fe-O bond distance which corresponds to the non-reactive Fe(IV)-oxo electronic configuration (open circles and squares, respectively) and to the radical Fe(III)-oxyl configuration (closed circles and squares, respectively). The vertical orange and black dotted lines on both figures indicate the Fe-O distance where the character of the electronic states changes from the non-reactive Fe(IV)-oxo to the radical Fe(III)-oxyl.

(NH<sub>3</sub>), while for the all-ammonia complex ([Fe(O)(NH<sub>3</sub>)<sub>4</sub>]<sup>2+</sup>), the  $\Delta E(^5A-^5E)$  at 1.60 Å is 1.79 eV. Similarly, the intercrossing of the two quintet states occurs at longer Fe-O bond distances once the strength of the ligand field increases (from 1.86 to 2.03 Å). Therefore, we conclude that the increase of the ligand field strength destabilizes the  $\pi$ -channel (Figure 9) and makes it less accessible for C-H activation. This conclusion is in agreement with the observation made by Kupper *et al.*<sup>40</sup> on the reactivity of the [Fe(O)(TMC)(MeCN)]<sup>2+</sup> biomimetic model complex that shares the same coordination environment with the [Fe(O)(H<sub>2</sub>O)<sub>ax</sub>(NH<sub>3</sub>)<sub>4</sub>]<sup>2+</sup> complex from our study. In the previous study, a combination of DFT with multiconfigurational calculations revealed that the specific non-heme model complex has only one accessible reaction mechanism (<sup>5</sup> $\sigma$ ).

Table 1: Energy difference  $\Delta E$  (eV) of the <sup>5</sup>E and lowest triplet states (<sup>3</sup>A/<sup>3</sup>E) with respect to the most stable quintet state (<sup>5</sup>A) at  $R_{Fe-O} = 1.60$  Å, Fe-O distance  $R_c$  (Å) where <sup>5</sup>A and <sup>5</sup>E states cross, and  $R_{c,Q/T}$  (Å) where quintet and triplet states cross.

Model Complex	$\Delta E(^5E)$	$\Delta E(^3A/^3E)$	$R_c$	$R_{c,Q/T}$
[Fe(O)(H <sub>2</sub> O) <sub>4</sub> ] <sup>2+</sup>	1.31	1.73	1.91	1.92
[Fe(O)(H <sub>2</sub> O) <sub>5</sub> ] <sup>2+</sup>	1.24	1.42	1.86	1.97
[Fe(O)(H <sub>2</sub> O) <sub>ax</sub> (NH <sub>3</sub> ) <sub>3</sub> ] <sup>2+</sup>	1.56	1.69	1.97	1.92
[Fe(O)(H <sub>2</sub> O) <sub>ax</sub> (NH <sub>3</sub> ) <sub>4</sub> ] <sup>2+</sup>	1.65	-0.46	1.98	2.10
[Fe(O)(NH <sub>3</sub> ) <sub>4</sub> ] <sup>2+</sup>	1.79	2.26	2.03	1.94
[Fe(O)(NH <sub>3</sub> ) <sub>5</sub> ] <sup>2+</sup>	1.92	-0.47	2.03	2.10

From the six model complexes discussed, the [Fe(O)(H<sub>2</sub>O)<sub>ax</sub>(NH<sub>3</sub>)<sub>4</sub>]<sup>2+</sup> and [Fe(O)(NH<sub>3</sub>)<sub>5</sub>]<sup>2+</sup> have a triplet ground state (<sup>3</sup>E). However, the specific complex follows a two-state reactivity mechanism,<sup>72</sup> so the quintet states are mostly relevant to C-H activation. For examining the accessibility of the <sup>3</sup> $\sigma$  and <sup>3</sup> $\pi$  channels, we have analyzed the character of the triplet states and how those evolve to Fe(III)-oxyl with hole on the  $\sigma$  and  $\pi$  bonding orbitals, respectively. For all species, six low-lying triplet states were found, which are within less than 1.0 eV for the Fe-O bond range of 1.6-1.9 Å. The only exception are [Fe(O)(H<sub>2</sub>O)<sub>ax</sub>(NH<sub>3</sub>)<sub>4</sub>]<sup>2+</sup> and [Fe(O)(NH<sub>3</sub>)<sub>5</sub>]<sup>2+</sup> which due to Jahn-Teller effect (Figure 2(b)) have a non-degenerate triplet ground state, with the next three triplet states being more than 1.39 eV less stable (at 1.60 Å).

Finally, for all the models considered in this study, the ground state (quintet) crosses the triplet states at bond distances that all channels are accessible (1.92-1.97 Å, Table 1). Exceptions are the two species with inverted spin state order (intercrossing at 2.10 Å), but since they follow the two-state reactivity scheme, the quintet states are more relevant for comparison.

## V. Conclusions and Outlook

In this work, we have performed an in-depth study on the electronic structure of the low-lying states of a bare FeO<sup>2+</sup> species and a series of six Fe(IV)-oxo model complexes, by applying multiconfigurational wave function theory. Our calculations revealed the electronic effects of the strength of the ligand field on the most stable quintet and triplet states, and were correlated to the reaction channels of the evolving Fe(III)-

oxyl radical species for C-H activation. The results presented here suggest that engineering of the primary coordination sphere can tune the accessibility of the different C-H reaction channels of the Fe(IV)-oxo biomimetic sites and affect their reactivity.

The electronic structure of naked iron oxide dication was elucidated via the construction of full PECs and the analysis of the equilibrium configurations at highly correlated multi-reference techniques (CASSCF and MRCI). We found potential energy minima in two different Fe-O regions. At longer distances (2-2.5 Å) an iron-oxyl (radical oxygen terminal) character prevails while at shorter distances the iron-oxo (closed-shell oxygen terminal) character emerges. It is the <sup>5</sup> $\Sigma^+$  and <sup>5</sup> $\Pi$  states which evolve to <sup>5</sup>A and <sup>5</sup>E ones species upon coordination, which exhibit an Fe(III)-O<sup>-</sup> and Fe(IV)-O<sup>2-</sup> identity

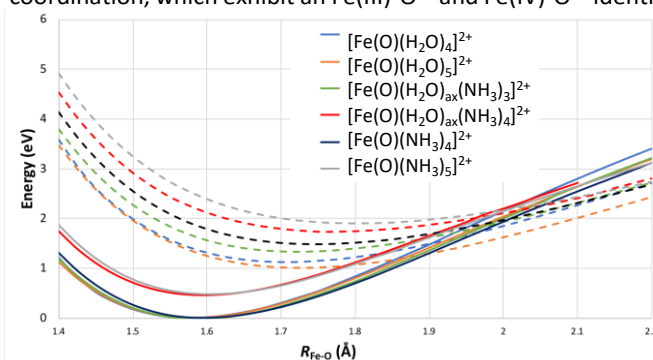


Figure 9: Superimposed potential energy curves of the six Fe-oxo models considered in this study. Solid lines correspond to the ground quintet state (<sup>5</sup>A) that evolves to the <sup>5</sup> $\sigma$  channel, dashed lines to the first excited state (<sup>5</sup>E) that evolves to the <sup>5</sup> $\pi$  channel.

at longer and shorter Fe-O distances, respectively. For all states we report accurate energetics and spectroscopic parameters. Despite its metastable nature, bare FeO<sup>2+</sup> is separated from the Fe<sup>+</sup>O<sup>+</sup> fragments by large activation barriers enabling its experimental observation.

Once the electronic structure of the bare FeO<sup>2+</sup> was elucidated, we examined the ligand field effects on the low-lying states. At the equilibrium geometry, the [FeOL<sub>n</sub>]<sup>2+</sup> species (L = H<sub>2</sub>O and/or NH<sub>3</sub>, n = 4 or 5) have a non-reactive Fe(IV)-oxo character, that evolves into a Fe(III)-oxyl radical once at larger Fe-O bond distances. The radical character is a consequence of an electron promotion from the bonding  $\sigma$  or  $\pi$  orbitals to the antibonding ones. Since the bonding orbitals are polarized towards the oxygen atom, that electron transfer is responsible for the formation of a hole on the 2p atomic orbitals of the oxygen, which evolves the radical character. This electron hole on oxygen can be found either on the  $\sigma$ - or  $\pi$ -type orbital, which are responsible for different C-H abstraction mechanisms, known as  $\sigma$ - and  $\pi$ -mechanisms, respectively. In this work, we quantified the accessibility of those reaction channels by considering different ligand field environments. We have considered the relative energy difference of the two states responsible for these two reaction channels, and the Fe-O bond distance that they intercross.

The Fe(IV)-oxo sites that have multiple accessible reaction channels are considered more catalytically active than those that have only one channel for C-H activation. We showed that a weaker ligand environment lowers the energy difference

between the reactive states of the Fe(IV)-oxo species at the equilibrium geometry, which will evolve into Fe(III)-oxyl with strong radical character, and eventually increases their reactivity. Conclusions from the multiconfigurational calculations presented in this work are in agreement with recent literature and support the known structure-function relation between ligand field strength and catalytic performance for C-H activation.<sup>16,75</sup> For example, Mukherjee *et al.* have reported a 10<sup>4</sup>-fold increase of oxidation reaction rates when weaker ligands are introduced in equatorial position in a Fe(IV)-oxo complex.<sup>76</sup> We believe that in the future, the relative energies of the ground ( $\sigma$ -mechanism) and first excited states ( $\pi$ -mechanism) can be used as a descriptor of catalytic activity of the Fe(IV)-oxo species.

### Conflicts of interest

There are no conflicts to declare.

### Acknowledgements

J. K. K., B. C. and K.D.V. would like to acknowledge the University of Tennessee for financial support of this work (start-up grant). This material is based upon work partially supported by the National Science Foundation under Grant No. CHE-1800237 (J. K. K., K.D.V.). S. N. K and E. M. are indebted to Auburn University for financial support. This work was conducted using the Advanced Computer Facility of the University of Tennessee and the Auburn University Hopper Cluster computational resources.

### References

1. H. Schwarz, *Angew. Chem. Int. Ed.*, 2011, **50**, 10096.
2. F. Roudesly, J. Oble and G. Poli, *J. Mol. Catal. A: Chem*, 2017, **426**, 275.
3. H. Schwarz, S. Shaik and J. Li, *J. Am. Chem. Soc.*, 2017, **139**, 17201.
4. H. Schwarz, P. González-Navarrete, J. Li, M. Schlangen, X. Sun, T. Weiske and S. Zhou, *Organometallics*, 2016, **36**, 8.
5. T. L. Poulos, *Chem. Rev.*, 2014, **114**, 3919.
6. K. Ray, F. F. Pfaff, B. Wang and W. Nam, *J. Am. Chem. Soc.*, 2014, **136**, 13942.
7. S. Sahu and D. P. Goldberg, *J. Am. Chem. Soc.*, 2016, **138**, 11410.
8. J. M. Elkins, M. J. Ryle, I. J. Clifton, J. C. D. Hotopp, J. S. Lloyd, N. I. Burzlaff, J. E. Baldwin, R. P. Hausinger and P. L. Roach, *Biochemistry*, 2002, **41**, 5185.
9. J. C. Price, E. W. Barr, T. E. Glass, C. Krebs and J. M. Bollinger Jr., *J. Am. Chem. Soc.*, 2003, **125**, 13008.
10. M. L. Matthews, C. S. Neumann, L. A. Miles, T. L. Grove, S. J. Booker, C. Krebs, C. T. Walsh and J. M. Bollinger Jr., *Proc. Natl. Acad. Sci.*, 2009, **106**, 17723.
11. S. D. Wong, M. Srnc, Megan L. Matthews, L. V. Liu, Y. Kwak, K. Park, C. B. Bell III, E. E. Alp, J. Zhao, Y. Yoda, S. Kitao, M. Seto, C. Krebs, J. M. Bollinger and E. I. Solomon, *Nature*, 2013, **499**, 320.
12. C. Krebs, D. G. Fujimori, C. T. Walsh and J. M. Bollinger Jr., *Acc. Chem. Res.*, 2007, **40**, 484.
13. B. E. Eser, E. W. Barr, P. A. Frantom, L. Saleh, J. M. Bollinger Jr., C. Krebs and P. F. Fitzpatrick, *J. Am. Chem. Soc.*, 2007, **129**, 11334.
14. D. G. Fujimori, E. W. Barr, M. L. Matthews, G. M. Koch, J. R. Yonce, C. T. Walsh, J. M. Bollinger Jr., C. Krebs and P. J. Riggs-Gelasco, *J. Am. Chem. Soc.*, 2007, **129**, 13408.
15. M. L. Matthews, C. M. Krest, E. W. Barr, F. H. Vaillancourt, C. T. Walsh, M. T. Green, C. Krebs and J. M. Bollinger Jr., *Biochemistry*, 2009, **48**, 4331.
16. W. Nam, *Acc. Chem. Res.*, 2007, **40**, 522.
17. L. Que Jr., *Acc. Chem. Res.*, 2007, **40**, 493.
18. W. N. Oloo and L. Que, *Acc. Chem. Res.*, 2015, **48**, 2612.
19. M. Puri and L. Que, *Acc. Chem. Res.*, 2015, **48**, 2443.
20. W. Nam, *Acc. Chem. Res.*, 2015, **48**, 2415.
21. V. I. Sobolev, K. A. Dubkov, O. V. Panna and G. I. Panov, *Catal. Today*, 1995, **24**, 251.
22. K. A. Dubkov, V. I. Sobolev, E. P. Talsi, M. A. Rodkin, N. H. Watkins, A. A. Shteinman and G. I. Panov, *J. Mol. Catal. A: Chem*, 1997, **123**, 155.
23. B. E. R. Snyder, P. Vanelderen, M. L. Bols, S. D. Hallaert, L. H. Böttger, L. Ungur, K. Pierloot, R. A. Schoonheydt, B. F. Sels and E. I. Solomon, *Nature*, 2016, **536**, 317.
24. D. J. Xiao, E. D. Bloch, J. A. Mason, W. L. Queen, M. R. Hudson, N. Planas, Joshua Borycz, A. L. Dzubak, P. Verma, K. Lee, F. Bonino, V. Crocellà, J. Yano, S. Bordiga, D. G. Truhlar, L. Gagliardi, C. M. Brown and J. R. Long, *Nature. Chem.*, 2014, **6**, 590.
25. P. Liao, R. B. Getman and R. Q. Snurr, *ACS Appl. Mater. Interfaces*, 2017, **9**, 33484.
26. P. Verma, K. D. Vogiatzis, N. Planas, J. Borycz, D. J. Xiao, J. R. Long, L. Gagliardi and D. G. Truhlar, *J. Am. Chem. Soc.*, 2015, **137**, 5770.
27. H. Hirao, W. K. H. Ng, A. M. P. Moeljadi and S. Bureekaew, *ACS Catal.*, 2015, **5**, 3287.
28. X. Engelmann, I. Monte-Pérez and K. Ray, *Angew. Chem. Int. Ed.*, 2016, **55**, 7632.
29. J. England, Marlène Martinho, E. R. Farquhar, J. R. Frisch, E. L. Bominaar, E. Münck and L. Que, *Angew. Chem. Int. Ed.*, 2009, **48**, 3622.
30. D. C. Lacy, R. Gupta, K. L. Stone, J. Greaves, J. W. Ziller, M. P. Hendrich and A. S. Borovik, *J. Am. Chem. Soc.*, 2010, **132**, 12188.
31. J. P. Bigi, W. H. Harman, B. Lassalle-Kaiser, D. M. Robles, T. A. Stich, J. Yano, R. D. Britt and C. J. Chang, *J. Am. Chem. Soc.*, 2012, **134**, 1536.
32. J. England, Y. Guo, K. M. V. Heuvelen, M. A. Cranswick, G. T. Rohde, E. L. Bominaar, E. Münck and L. Que, *J. Am. Chem. Soc.*, 2011, **133**, 11880.
33. A. N. Biswas, M. Puri, K. K. Meier, W. N. Oloo, G. T. Rohde, E. L. Bominaar, E. Münck and L. Que Jr., *J. Am. Chem. Soc.*, 2015, **137**, 2428.
34. O. Pestovsky, S. Stoian, E. L. Bominaar, X. Shan, E. Münck, L. Que Jr. and A. Bakac, *Angew. Chem. Int. Ed.*, 2005, **44**, 6871.
35. M. B. Chambers, S. Groysman, D. Villagrán and D. G. Nocera, *Inorg. Chem.*, 2013, **52**, 3159.
36. D. Schröder, S. Shaik and H. Schwarz, *Acc. Chem. Res.*, 2000, **33**, 139.
37. S. Shaik, H. Chen and D. Janardanan, *Nat. Chem.*, 2011, **3**, 19.
38. S. Meyer, I. Klawitter, S. Demeshko, E. Bill and F. Meyer, *Angew. Chem. Int. Ed.*, 2013, **52**, 901.
39. S. Ye, C. Kupper, S. Meyer, E. Andris, R. Navrátil, O. Krahe, B. Mondal, M. Atanasov, E. Bill, J. Roithová, F. Meyer and F. Neese, *J. Am. Chem. Soc.*, 2016, **138**, 14312.
40. C. Kupper, B. Mondal, J. Serrano-Plana, I. Klawitter, F. Neese, M. Costas, S. Ye and F. Meyer, *J. Am. Chem. Soc.*, 2017, **139**, 8939.

41. R. Kumar, A. Ansari and G. Rajaraman, *Chem. Eur. J.*, 2018, **24**, 6818.
42. M. Srncic, S. D. Wong, J. England, J. Lawrence Que and E. I. Solomon, *Proc. Natl. Acad. Sci.*, 2012, **109**, 14326.
43. M. Srncic, S. D. Wong, M. L. Matthews, C. Krebs, J. M. Bollinger Jr. and E. I. Solomon, *J. Am. Chem. Soc.*, 2016, **138**, 5110.
44. A. Decker, J.-U. Rohde, E. J. Klinker, S. D. Wong, J. Que, Lawrence and E. I. Solomon, *J. Am. Chem. Soc.*, 2007, **129**, 15983.
45. M. Srncic, S. D. Wong and E. I. Solomon, *Dalton Trans.*, 2014, **43**, 17567.
46. S. Ye and F. Neese, *Proc. Natl. Acad. Sci.*, 2011, **108**, 1228.
47. B. K. Mai and Y. Kim, *Inorg. Chem.*, 2016, **55**, 3844.
48. D. Usharani, D. Janardanan, C. Li and S. Shaik, *Acc. Chem. Res.*, 2013, **46**, 471.
49. J. England, Y. Guo, E. R. Farquhar, V. G. Young Jr., E. Münck and L. Que Jr., *J. Am. Chem. Soc.*, 2010, **132**, 8635.
50. M. L. Neidig, A. Decker, O. W. Choroba, F. Huang, M. Kavana, G. R. Moran, J. B. Spencer and E. I. Solomon, *Proc. Natl. Acad. Sci.*, 2006, **103**, 12966.
51. D. Fang, R. L. Lord and G. A. Cisneros, *J. Phys. Chem. B*, 2013, **117**, 6410.
52. J. Olsen, B. O. Roos, P. Jørgensen and H. J. A. Jensen, *J. Chem. Phys.*, 1988, **89**, 2185.
53. B. O. Roos, P. R. Taylor and P. E. M. Siegbahn, *Chem. Phys.*, 1980, **48**, 157.
54. P. J. Knowles and H.-J. Werner, *Chem. Phys. Lett.*, 1988, **145**, 514.
55. H. J. Werner and P. J. Knowles, *J. Chem. Phys.*, 1988, **89**, 5803.
56. K. Andersson, P. Å. Malmqvist and B. O. Roos, *J. Chem. Phys.*, 1992, **96**, 1218.
57. H.-J. Werner, P. J. Knowles, G. Knizia, F. R. Manby, M. Schütz, P. Celani, T. Korona, R. Lindh, A. Mitrushenkov, G. Rauhut, K. R. Shamasundar, T. B. Adler, R. D. Amos, A. Bernhardsson, A. Berning, D. L. Cooper, M. J. O. Deegan, A. J. Dobson, F. Eckert, E. Goll, C. Hampel, A. Hesselmann, G. Hetzer, T. Hrenar, G. Jansen, C. Köppl, Y. Liu, A. W. Lloyd, R. A. Mata, A. J. May, S. J. McNicholas, W. Meyer, M. E. Mura, A. Nicklass, D. P. O'Neill, P. Palmieri, D. Peng, K. Pflüger, R. Pitzer, M. Reiher, T. Shiozaki, H. Stoll, A. J. Stone, R. Tarroni, T. Thorsteinsson and M. Wang, *MOLPRO, version 2012.1, a package of ab initio programs*, University College Cardiff Consultants, Ltd.: Cardiff, U.K., 2012.
58. P. Å. Malmqvist, A. Rendell and B. O. Roos, *J. Phys. Chem.*, 1990, **94**, 5477.
59. P. Å. Malmqvist, K. Pierloot, A. R. M. Shahi, C. J. Cramer and L. Gagliardi, *J. Phys. Chem.*, 2008, **112**, 204109.
60. F. Aquilante, J. Autschbach, R. K. Carlson, L. F. Chibotaru, M. G. Delcey, L. D. Vico, I. F. Galván, N. Ferré, L. M. Frutos, L. Gagliardi, M. Garavelli, A. Giussani, C. E. Hoyer, G. L. Manni, H. Lischka, D. Ma, P. Å. Malmqvist, T. Müller, A. Nenov, M. Olivucci, T. B. Pedersen, D. Peng, F. Plasser, B. Pritchard, M. Reiher, I. Rivalta, I. Schapiro, J. Segarra-Martí, M. Stenrup, D. G. Truhlar, L. Ungur, A. Valentini, S. Vancoillie, V. Veryazov, V. P. Vysotskiy, O. Weingart, F. Zapata and R. Lindh, *J. Comput. Chem.*, 2016, **37**, 506.
61. B. O. Roos, R. Lindh, P.-Å. Malmqvist, V. Veryazov and P.-O. Widmark, *J. Phys. Chem. A*, 2004, **108**, 2851.
62. B. O. Roos, R. Lindh, P.-Å. Malmqvist, V. Veryazov and P.-O. Widmark, *J. Phys. Chem. A*, 2005, **109**, 6575.
63. M. Douglas and N. M. Kroll, *Ann. Phys.*, 1974, **82**, 89.
64. B. A. Hess, *Phys. Rev. A*, 1986, **33**, 3742.
65. G. Ghigo, B. O. Roos and P.-Å. Malmqvist, *Chem. Phys. Lett.*, 2004, **396**, 142.
66. N. Forsberg and P. Å. Malmqvist, *Chem. Phys. Lett.*, 1997, **274**, 196.
67. F. Aquilante, R. Lindh and T. B. Pedersen, *J. Chem. Phys.*, 2007, **127**, 114107.
68. S. Vancoillie, H. Zhao, V. T. Tran, M. F. A. Hendrickx and K. Pierloot, *J. Chem. Theory Comput.*, 2011, **7**, 3961.
69. C. N. Sakellaris, E. Miliordos and A. Mavridis, *J. Chem. Phys.*, 2011, **134**, 234308.
70. CRC Handbook of Chemistry and Physics. ed. W. M. Haynes, Taylor and Francis, Boca Raton, FL, 93th ed., 2012.
71. A. Kramida, Y. Ralchenko and J. Reader, 2018, NIST Atomic Spectra Database (ver. 5.5.6), <http://physics.nist.gov/asd> National Institute of Standards and Technology, Gaithersburg, MD.
72. A. Kazaryan and E. J. Baerends, *ACS Catal.*, 2015, **5**, 1475.
73. K. Pierloot, Q. M. Phung and A. Domingo, *J. Chem. Theory Comput.*, 2017, **13**, 537.
74. M. Radoń and K. Pierloot, *J. Phys. Chem. A*, 2008, **112**, 11824.
75. J. England, G. J. Britovsek, N. Rabadia and A. J. White, *Inorg. Chem.*, 2007, **46**, 3752.
76. G. Mukherjee, C. W. Z. Lee, S. S. Nag, A. Alili, F. G. Cantu Reinhard, D. Kumar, C. V. Sastri and S. P. de Visser, *Dalton Trans.*, 2018.

## Graphical Abstract (Table of Contents Entry)

